# Delft University of Technology

## A Stand-Alone Si-Based Porous Photoelectrochemical Cell

Vijselaar, Wouter J.C.; Perez-Rodriguez, Paula; Westerik, Pieter J.; Tiggelaar, Roald M.; Smets, Arno H.M.; Gardeniers, Han; Huskens, Jurriaan

**Important note**
To cite this publication, please use the final published version (if applicable).
Please check the document version above.

FULL PAPER

Solar Water Splitting

ADVANCED
ENERGY
MATERIALS

www.advenergymat.de

# A Stand-Alone Si-Based Porous Photoelectrochemical Cell

Wouter J. C. Vijselaar, Paula Perez-Rodriguez, Pieter J. Westerik, Roald M. Tiggelaar, Arno H. M. Smets, Han Gardeniers,* and Jurriaan Huskens*

Wireless photoelectrochemical (PEC) devices promise easy device fabrication as well as reduced losses. Here, the design and fabrication of a stand-alone ion exchange material-embedded, Si membrane-based, photoelectrochemical cell architecture with micron-sized pores is shown, to overcome the i) pH gradient formation due to long-distance ion transport, ii) product crossover, and iii) parasitic light absorption by application of a patterned catalyst. The membrane-embedded PEC cell with micropores utilizes a triple Si junction cell as the light absorber, and Pt and IrO$_x$ as electrocatalysts for the hydrogen evolution reactions and oxygen evolution reactions, respectively. The solar-to-hydrogen efficiency of 7% at steady-state operation, as compared to an unpatterned $\eta_{PV}$ of 10.8%, is mainly attributed to absorption losses by the incorporation of the micropores and catalyst microdots. The introduction of the Nafion ion exchange material ensures an intrinsically safe PEC cell, by reducing the total gas crossover to <0.1%, while without a cation exchange membrane, a crossover of >6% is observed. Only in a pure electrolyte of 1 M H$_2$SO$_4$, a pH gradient-free system is observed thus completely avoiding the build-up of a counteracting potential.

Dr. W. J. C. Vijselaar, Prof. J. Huskens
Molecular NanoFabrication
MESA+ Institute for Nanotechnology
University of Twente
P.O. Box 217, 7500 AE Enschede, The Netherlands
E-mail: j.huskens@utwente.nl
Dr. P. Perez-Rodriguez, Prof. A. H. M. Smets
Photovoltaic Materials and Devices Laboratory
Electrical Engineering
Mathematics and Computer Science Faculty
Delft University of Technology
P.O. Box 5031, 2600 GA Delft, The Netherlands
Dr. P. J. Westerik, Prof. J. G. E. (Han) Gardeniers
Mesoscale Chemical Systems
MESA+ Institute for Nanotechnology
University of Twente
P.O. Box 217, 7500 AE Enschede, The Netherlands
E-mail: j.g.e.gardeniers@utwente.nl
Dr. R. M. Tiggelaar
NanoLab Cleanroom
MESA+ Institute for Nanotechnology
University of Twente
P.O. Box 217, 7500 AE Enschede, The Netherlands

## 1. Introduction

Development of a photoelectrochemical (PEC) cell has received increasing attention for large-scale solar energy conversion and storage applications. The primary components of a stand-alone PEC cell include photoabsorbers, electrocatalysts, membrane separators, electrolytes, and the supporting structures. In short, photoabsorbers capture and convert the incident photons and generate the required photovoltage and photocurrent to drive the required fuel-forming reactions. Electrocatalysts lower the kinetic overpotentials and therefore affect the solar-to-hydrogen (STH) and selectivity of the fuel-forming reactions. A membrane separator prevents product crossover, thus avoiding explosive/flammable product mixtures (e.g., H$_2$/O$_2$ mixtures). Last, the electrolyte facilitates ion transport between the cathode and anode compartments and provides the water/reactant. To develop an efficient and intrinsically safe PEC cell, among others, the following cell parameters need to be minimized simultaneously: i) concentration-overpotential losses, ii) electrolyte resistive losses, iii) the rates of gas crossover, and iv) parasitic light absorption by the catalyst, the last of which is negatively correlated with the light-limited photocurrent.[1]

The thermodynamic voltage to split water in a PEC cell is 1.23 V.[2] The upper limit on the tolerable losses strongly depends on the photoabsorber characteristics. For example, if the PEC device is driven by a state-of-the-art PV cell operating at maximum power with a voltage of ($V_{mp}$) ≈1.7 V at a current density ($J_{sc}$) of 10 mA cm$^{-2}$ then the maximum tolerable potential loss can be only ≈500 mV.[3] The overpotentials needed to drive the hydrogen and oxygen evolution reaction at 10 mA cm$^{-2}$ added together are already at least 400 mV, respectively, as reported by McCrory et al.[4] Thus, all other potential losses should be within the range of 100 mV, to achieve a STH efficiency of at least 10%.

The constraints mentioned above affect geometric design parameters in a conflicting manner. The design parameters for the construction of a PEC cell have been modeled extensively with respect to: the optimal band gap combination for photoabsorbers, the overall kinetic overpotential for electrocatalysts, the permeability and conductivity properties for membrane separators, and the conductivity and pH requirements for the electrolyte solution.[1,5] Although these simulations help tremendously to pave the way toward efficient PEC cells, practical measurements

**ADVANCED
SCIENCE NEWS**

www.advancedsciencenews.com

**ADVANCED
ENERGY
MATERIALS**

www.advenergymat.de

are essential to explore the actual geometric design parameters to fabricate a full stand-alone PEC cell.

Within the discussion of possible device concepts, both wired and wireless devices are envisioned as possible contenders.[6] The wireless design has the upper hand, first of all, due to the simplified cell design by eliminating electrical contacts and wires through integration of all components in a flat assembly.[7] More importantly, electronic conductivity is much higher ($\approx 10^5$ S cm$^{-1}$) than ionic conductivity (<1 S cm$^{-1}$). Therefore, Newman showed by a simple analysis that, in order to keep Ohmic losses within the device low, a short ionic pathway between the two electrodes is a necessity.[8] LeRoy et al. pointed out that for a wired device an increase of gas volume between the electrodes (i.e., at a short electrode distance) will lead to a higher electrical resistance, an efficiency decrease of water electrolysis, and the lodging of bubbles between the electrodes.[9] A wireless device overcomes these problems, by separating the production of the evolved gasses in two separate compartments. However, in a wireless device short ionic pathways between the anode and cathode are still required to reduce the overall resistance.

Bosserez et al. investigated a porous monolith for reducing the ionic pathway of (not photoactive) silicon electrodes with micron-sized pores, with the aim to provide ionic shortcuts and gain more insight into the potential losses due to the electrolyte. A loss of less than 100 mV was found at 7.84 mA cm$^{-2}$ in 1 M KOH at a porosity of $\approx 7\%$ and a micropore pitch of 250 µm.[10] However, two problems evolved for this conceptual device. First, a substantial H$_2$ crossover of $\approx 20\%$ to the O$_2$ compartment was measured. Whether the crossover occurred by mass transfer of dissolved gasses or by transport of bubbles was not elucidated. The observed gas crossover is far above the lower flammable limit (4% H$_2$ in the O$_2$ compartment) and the lower explosion limit (17% H$_2$ in the O$_2$ compartment), and therefore not intrinsically safe nor useful in a functioning solar-to-fuel device.[11] Second, a possible change of local pH around the electrodes, causing a pH gradient, was not considered, while these pH gradients can amount to a severe increase in required potential to drive the reaction.[12]

To reduce the crossover of reaction products to below the flammable limit, micropores as proposed by Bosserez et al. may be filled with a molecular barrier material (e.g., a cation or anion exchange material) to prevent crossover of gaseous products, while maintaining proton (or hydroxide) transfer. However, such a membrane introduces a new problem, as was shown by Hernández-Pagán et al.[12] These authors measured a large pH difference developed between the anode and cathode compartments, originally filled with near-neutral pH electrolytes, in an electrolysis cell (in a wired configuration), where the compartments were separated by either an anion or cation exchange membrane, which led to an extra required potential up to 341 mV within 6 h of operation.[12] Even with simulated diurnal cycling (i.e., electrolysis cell 8 h on, 16 h off), a significant pH gradient remained after three cycles.[12] Modestino et al. have confirmed this finding by showing that circulation of the anode and cathode compartments in a near-neutral electrolyte was an absolute necessity, otherwise the performance of their wired PEC device rapidly came to a halt.[13] A pump was required to perform this circulation, which required energy to operate, and thus suppressed the overall obtainable STH

efficiency. Singh et al. simulated a wired device in a strong acid (e.g., 0.1 M H$_2$SO$_4$) in combination with a cation exchange membrane and showed the rapid formation of a pH gradient at operating current densities >8 mA cm$^{-2}$.[1] However, to date no practical data have been presented on the existence and in situ formation of a pH gradient for a wireless porous PEC device configuration, with an ion exchange material incorporated.

Another point of concern is that electrocatalysts block the incoming solar light and thereby reduce the overall generated photocurrent, and thus the fuel production. Chen et al. showed that patterning electrocatalysts on the surface of photoabsorbers in a solar-fuel generator could provide a viable approach to minimize the parasitic light absorption by catalyst films and still maintain a high overall $\eta_{PV}$.[14] However, from an experimental point of view this study only presented the dependence of the catalytic activity on the filling fraction of the catalyst on the surface, without taking the effects of the underlying PV cell into account.

Trompoukis et al. investigated the impact of porosity on the PV cell parameters of single, tandem, and triple PV cells.[15] They found the efficiency of the underlying PV cell to be mainly affected by a substantial decrease of the fill factor, while the open circuit potential and short circuit density were less affected. However, their modeling of the influence of catalyst addition was not experimentally verified.

All of these studies have presented significant results to solve one or more of the requirements to produce an efficient and intrinsically safe PEC cell. Here, we show the design and fabrication of a stand-alone ion exchange material-embedded, membrane-based, photoelectrochemical cell architecture with micron-sized pores, to overcome all of the above stated drawbacks, such as pH gradient formation due to long-distance ion transport, parasitic light absorption, and product crossover. We employ a Si membrane with micropores, in which a thin film of a cation exchange material in placed. Micropatterning of the catalyst is performed at the illumination side to reduce parasitic light absorption losses, and the pitch of this pattern is varied to balance light absorption and catalyst activity. The influence of membrane porosity on the device performance is studied by experimental (photo)electrochemistry as well as by analytical and finite-element models.

## 2. Results and Discussion

**Figure 1**A shows the concept of the photoelectrochemical cell, based on a Si membrane with micropores, with an embedded cation exchange material. The starting substrate was an all Si photovoltaic triple cell, in order to generate sufficient potential for the oxygen evolution reactions (OER) and hydrogen evolution reactions (HER).[16] The top cell consisted of an amorphous silicon (a-Si:H) absorber (red), the middle cell used a nanocrystalline silicon (nc-Si:H) absorber (yellow), and the bottom cell was based on a monocrystalline silicon wafer (c-Si) with a silicon heterojunction (SHJ) structure (dark gray).[16] In order to reduce the overall ionic transport losses between the anode and cathode, micropores were etched through the triple PV cell.[10] The diameter of the micropores was set to 50 µm, and micropores with a pitch of 166 µm were etched into the triple PV cell by deep reactive etching (DRIE), as is shown in Figure 1B.
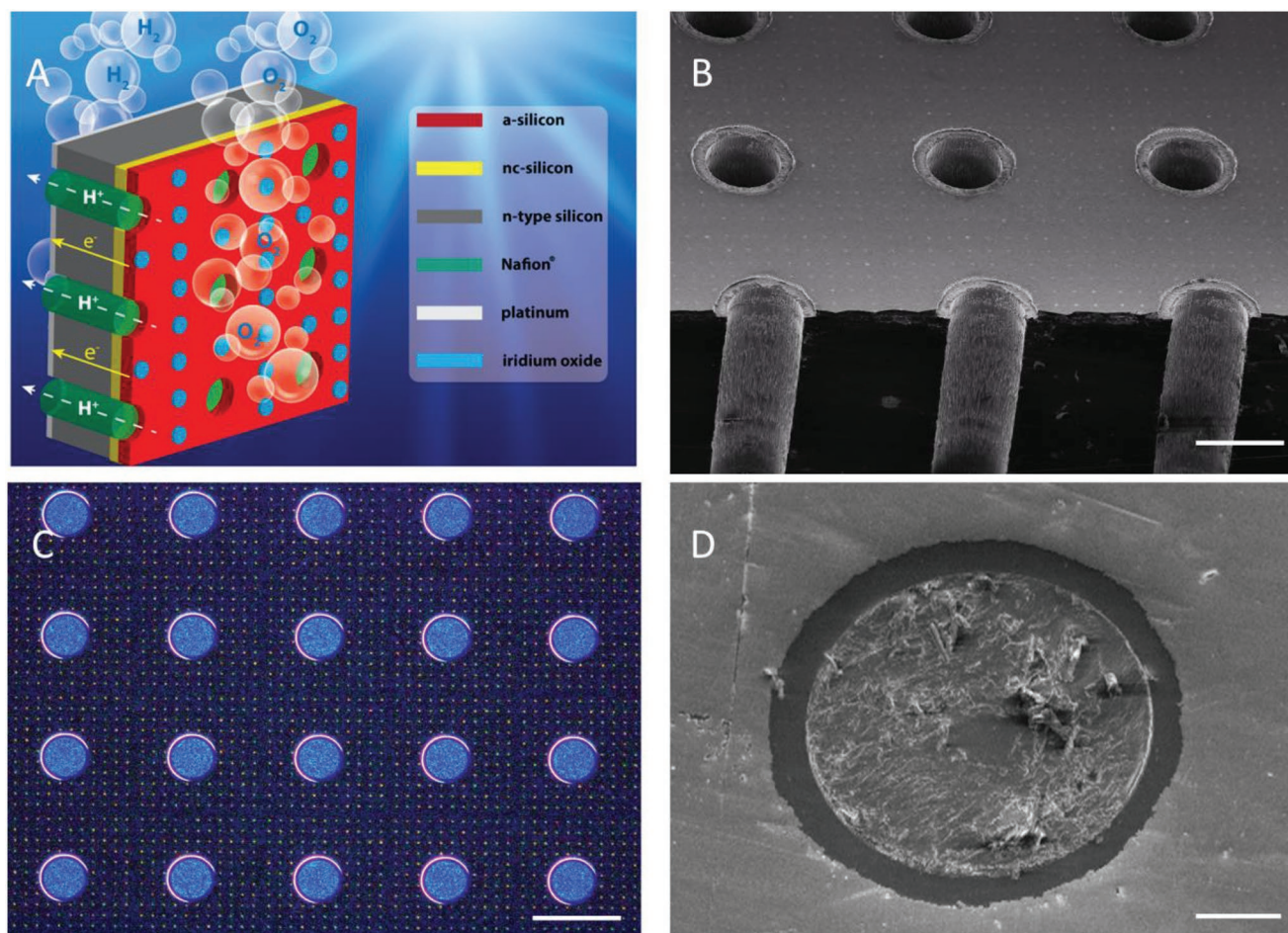
**Figure 1.** A) Schematically depicted stand-alone PEC cell, based on a Si membrane with micron-sized pores with embedded ion exchange material, highlighting the different components. B) Top view cross-sectional SEM (scale bar 50 μm) and C) light microscopy (scale bar 100 μm) images of the illuminated side (frontside of cartoon shown in (A)) of the stand-alone PEC cell with micropores (before filling with Nafion). Micropores (50 μm) were etched through the Si substrate (thickness 380 μm), at a pitch of 166 and 2 μm IrO$_x$ microdots are visible with a pitch of 16 μm. D) SEM image of the non-illuminated side (backside of cartoon shown in (A)) of the stand-alone PEC cell zooming in on a micropore filled with a Nafion proton exchange material, and showing a homogeneous Pt layer around the micropore (scale bar 13 μm).

In this process, etching completely through the Si substrate exposes bare silicon inside the micropores. Without protection, this would be etched very rapidly in an alkaline electrolyte.[17] Therefore, we performed our analysis in an acidic electrolyte to maintain stability of the silicon material. McCrory et al. benchmarked many known OER and HER catalysts in alkaline and acidic electrolytes and showed that the only stable and efficient combination in acidic electrolyte to date is iridium oxide (IrO$_x$) and platinum (Pt).[4] Therefore, we chose these electrocatalysts in our current membrane PEC cell. The illuminated side of the triple PV cell is p-type doped, and therefore IrO$_x$ was sputtered (and micropatterned) at the front side as OER catalyst, while a continuous layer of Pt as HER catalyst was placed at the backside. Chen et al. presented the importance of microdot arrays to minimize parasitic light absorption by the catalyst for the underlying light absorber (i.e., IrO$_x$ in our case) while maintaining sufficient catalyst activity. Therefore, we fabricated arrays of microdots of IrO$_x$, with a diameter of 2 μm and periodicities of 11, 16, and 22 μm, in order to evaluate the optimal balance between

light absorption and catalytic activity in the overall device. Arrays of micropores and IrO$_x$ microdots are clearly visualized in a light microscope image (Figure 1C) of the fabricated device. The small light blue dots are the micropatterned IrO$_x$ dots and the large blue circles are the micropores through-and-through the triple PV cell.

A molecular barrier material is required to separate the evolved gasses. Nafion, a per(fluorosulfonic acid) poly(tetrafluoroethylene) copolymer, is commonly used as the membrane separator material in proton exchange membrane fuel cells and can easily be dropcasted from various solvents.[18] A Nafion layer was dropcasted at the backside of the device, and excess Nafion was removed from the surface after solvent evaporation. As a result, Nafion was only present within the micropores. A close-up of the backside of Figure 1A is visualized in Figure 1D, here the surrounding (light gray) is Pt, with a circle around the micropore, and in the middle a filled micropore with Nafion. A cross-sectional SEM image is given in Figure S1, Supporting Information. The height of the Nafion membrane inside the holes is shown to vary slightly.
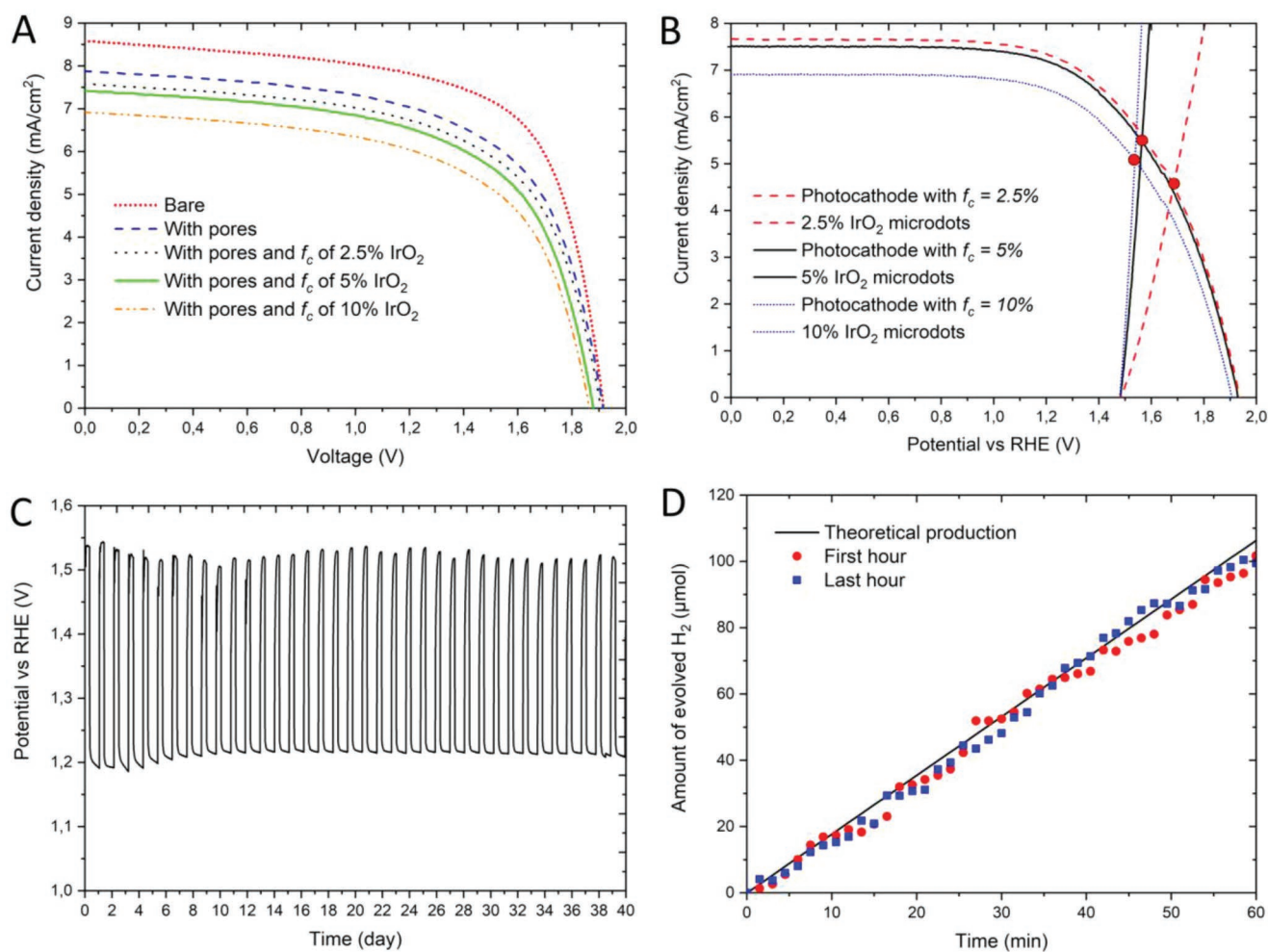
**Figure 2.** A) Photoelectrical $JV$ measurements on a bare solid state Si triple cell, a cell with 7% micropores, and microporous cells with a filling fraction of $IrO_x$ microdots of 2.5%, 5%, and 10%. B) Current density versus potential photocathode behavior for three different stand-alone, Nafion-embedded microporous PEC cells, with different filling fractions of catalyst (see Figure S2, Supporting Information, for the experimental setup). Overlay of the catalyst activity of the three different filling fractions of $IrO_x$, measured under AM 1.5 G and in 1 M $H_2SO_4$. Red dots indicate the stand-alone operating points (potential and current) at the different filling fractions of catalyst. C) Stability of the PEC cell as a water splitting device over the course of 33 days, with an induced light intermittency of 8 h on, 16 h off ($f_c$ 5%) (see Figure S3, Supporting Information, for the experimental setup). D) Produced hydrogen during the first and last hour of the stability test ($f_c$ of 5%), with a theoretical line when operated at 5.7 mA cm$^{-2}$.

## 2.1. Operational PEC Cell

We were able to fabricate one set of samples, and assess the impact of the fabrication on the samples. Both the micropores and $IrO_x$ microdots may result in PV absorption losses, which will be assessed here in more detail. **Figure 2**A shows the current–voltage characteristics of an unmodified (bare) triple Si PV cell before and after etching micropores through the cell. We observed only a slight decrease in the $V_{oc}$ of the bare triple PV cells when the micropores were incorporated. This small effect is most likely due to the passivation of the sidewalls of the micropores during fabrication. After etching the micropores through the Si triple PV cell, the surface was cleaned by $O_2$ plasma. This process is known to create a thin $SiO_2$ layer on bare Si surfaces, and $SiO_2$ is known to passivate the surface of Si PV cells. We have oberserved this effect before in the fabrication of microwire arrays, in which a nearly identical plasma etching procedure was followed.[19] For the case of the microwires, the surface area was increased 17 times, much more than in the present case of the micropores ($\approx$2.5$\times$), nevertheless we did not observe major differences in the $V_{oc}$ compared with flat PV cells.

It has been reported that exposure of silicon in the plasma, as was used here for etching the pores, can create (sub)surface damage and crystallographic defects that affect the charge carrier lifetimes.[20] This on its turn will have a negative effect on the $V_{oc}$. The fact that we do not observe evidence of this effect is surprising, even more so in light of the notion that the very thin silicon oxide layer, formed during the oxygen plasma treatment, will most likely not have sufficient passivating quality to compensate for the recombination sites introduced during RIE. We want to point out that Trompoukis et al.[15] have observed and explicitly noted a similar insensitivity of the $V_{oc}$ on the introduction of plasma-etched micropores (presumably also

without additional passivation layers). The explanation for this absence of the effect of plasma-induced damage, compared to the findings of Schaefer et al.[20] might be in differences in the interaction of ions and/or electrons originating from the plasma with the silicon surface in the etched structures: in our case the high-intensity, inductively coupled plasma is contained relatively far away from the surface, in Schaefer's case a parallel plate plasma reactor was used, where the high intensity plasma may be closer to the surface. Furthermore in Schaefer's case, any ion impact on the surface is perpendicular to the semiconductor layer that will be damaged, in our case, most of the surface of interest (the sidewalls of the pores) do not experience severe ion impact, and that might explain why plasma damage is less (and less important for the performance) in our case. The effect was not further analyzed here.

The $V_{oc}$ decreased further upon adding the $IrO_x$ microdots. We attributed this decrease to the observed decrease of the short circuit current density, because the micropores and $IrO_x$ microdots reduce the total surface area and block the incoming light, respectively, and therefore limit the light absorption capabilities. Indeed, the short-circuit current density decreased as well, from 8.5 to 7.9 mA cm$^{-2}$, due to a reduction in total surface area of photo-absorber caused by the formation of the micropores. This relative reduction of ≈7.1% agrees with the porosity (filling fraction) of 7% induced by the micropore formation. Upon introducing $IrO_x$ microdots on the microporous surface, a further decrease in current density was observed. Microdots (2 μm diameter) with a filling fraction of 2.5% (22 μm period), 5% (16 μm period), and 10% (11 μm period), led to a decrease of the current density to 7.6, 7.4, and 6.9 mA cm$^{-2}$, respectively. Here, the filling fraction ($f_c$) is defined as the ratio of the geometric area of the catalyst or micropores to the total geometric area of the photoelectrode. The measured current density values correspond to a decrease of 3.3%, 6.3%, and 11.7% compared to the microporous device without catalyst, respectively, which values agree reasonably well with the employed filling fractions of catalyst. All relevant values are summarized in **Table 1**.

The PEC performance of the device was characterized by operating the microporous device as a photocathode in a three-electrode voltammetry configuration (triple PV cell with the illuminated frontside as working electrode, Pt mesh counter electrode, and Ag/AgCl reference electrode, see Figure S2, Supporting Information) under AM 1.5G illumination from the $IrO_x$ side, in 1 M $H_2SO_4$. Figure 2B shows a plot of the current density obtained from the photocathode as a function of the applied potential. The obtained PEC current densities correspond well with the current densities obtained when measured as a PV cell (Figure 2A).

Chen et al. showed that low filling fractions (<10%) of, in their case Pt-based, catalyst islands did not lead to a significantly reduced performance of a cathode.[14] Therefore, we assessed the catalytic activity of the $IrO_x$ dots with different filling fractions (i.e., $f_c$ of 2.5%, 5%, and 10%) on top of Si, as seen in Figure 2B. The full characterization of the $IrO_x$ microdots is given in Figure S4, Supporting Information (schematic setup in Figure S5, Supporting Information). An $f_c$ of 2.5% of $IrO_x$ on top of Si showed a significantly reduced activity, as compared to a fully covered surface, most likely due to mass transport limitations, as suggested by Chen et al.[14] In contrast, filling fractions of 5% and 10% provided substantial activities, especially in the range up to 10 mA cm$^{-2}$. Compared to 100% coverage, ≈50% of the activity was retained when reducing the coverage to 5%.

Stand-alone operating current densities were obtained by overlaying the $JE$ relationship of the $IrO_x$ OER catalyst of Figure 2B (at $f_c$ values of 2.5%, 5%, or 10%). The obtained stand-alone current densities were 4.5, 5.7, and 5.1 mA cm$^{-2}$, for filling fractions of 2.5%, 5%, and 10% of $IrO_x$ microdots, respectively. Notably, although a higher filling fraction leads to a higher catalytic activity, the impact on the maximum current density was more severe for the overall efficiency when $f_c > 5\%$, due to stronger light blocking by the catalyst at the higher catalyst coverage. At $f_c < 5\%$, catalyst activity appears to be the limiting factor. Last, the increase in shunt resistance is attributed to an increase of surface passivation by the field effect. We employed a n-type Si wafer, and therefore electrons are shielded from the surface by upward band bending.[21] We do not expect that the band bending is affected by changes in the $SiO_2$ layer thickness during operation, because the electrochemical formation of $SiO_2$ occurs at a different potential (≈0.857 V vs E$^0$), and oxide formation caused by the strongly acidic electrolyte is limited to a few nanometer only,[22] which is below the oxide thickness already present after the $O_2$ plasma step. We specifically chose to compare to a PV cell to a photocathode, to show the direct comparison between $JV$ (Figure 2A) and $JE$ characterization (Figure 2B).

The electrolyte layer in front of the PEC cell did not lower the obtained current densities as compared to the PV cell. The electrolyte layers start to absorb light of wavelengths above 950 nm, therefore only the bottom cell is affected.[23] The bottom cell (≈17.1 mA cm$^{-2}$) produces a higher current density as compared to the top (8.5 mA cm$^{-2}$) and middle cells (≈9.2 mA cm$^{-2}$). Therefore, the top cell, which absorbs light up to ≈800 nm,[3] remains the limiting cell regarding the current density (see Experimental Section for more details).

We also measured the PEC cell as a photoanode and provide an overlay with a Pt cathode of the best performing cell (see Figure S6, Supporting Information, schematic setup in Figure S7, Supporting Information). The crossover point gives the same result as in Figure 2B, however a photo-anode is less comparable to a PV cell as was used in the analyses above. Furthermore, the current density output in the plateau region corresponds very well to the current density in Figure 2B, therefore the interference of the water layer in front of the PEC cell is most likely low, as discussed above.

**Table 1.** $JV$ characteristics for the various solid state triple PV cells shown in Figure 2A.

| Sample | $\eta_{PV}$ [%] | $J_{sc}$ [mA cm$^{-2}$] | $V_{oc}$ [V] | FF [%] |
|---|---|---|---|---|
| Bare | 10.8 | 8.57 | 1.92 | 66.17 |
| With pores | 9.3 | 7.86 | 1.90 | 62.09 |
| With pores and $f_c$ of 2.5% | 8.7 | 7.60 | 1.89 | 61.19 |
| With pores and $f_c$ of 5% | 8.5 | 7.42 | 1.87 | 61.18 |
| With pores and $f_c$ of 10% | 7.8 | 6.92 | 1.86 | 60.38 |

**ADVANCED**
**SCIENCE NEWS**
www.advancedsciencenews.com

**ADVANCED**
**ENERGY**
**MATERIALS**
www.advenergymat.de

We assessed the long-term PEC performance of the device (Figure 2C), and tested the hydrogen production by means of gas chromatography (Figure 2D), for the sample with the optimal $f_c$ of 5%. The gas production corresponds well with the observed current density of 5.7 mA cm$^{-2}$ (theoretical line in Figure 2D). During long-term PEC performance of the device, we monitored the open circuit potential of the anode versus a reference electrode (Figure 2C). In this fully integrated PEC cell it is not possible to directly measure the produced current density which flows through the cell. The PEC cell was tested under day-night cycles of 8 h light on and 16 h light off, thus mimicking the intermittency of the sun, see Figure 2C. Under illumination, the potential of the anode corresponded well to the potential of <1.6 V of the operating point, as depicted in Figure 2B. Upon switching the light off, the potential of the anode dropped to ≈1.2 V. This corresponds well to the open circuit potential of dissolved $O_2$ and $H_2$ gasses in contact with their respective metallic electrodes within the cell at the anode and cathode. Most importantly, the data in Figure 2C indicates that prolonged activity of the device over a month is possible without noticeable degradation. Hereafter, we tested again (Figure 2D) the gas production of the PEC cell, which still agrees well with the theoretical line of 5.7 mA cm$^{-2}$. An overall STH efficiency of 7% was obtained for the stand-alone device.

Fluctuations in hydrogen production over time are visible in Figure 2D, which is based on measurements at intervals of about ≈130 s. The reason for these fluctuations might be, despite the stirring that was performed during these tests, the irregular accumulation and detachment of gas bubbles at the anode and cathode surfaces, reducing either the active surface area for electrolysis and/or the available anode area for light absorption, which is translated in a temporarily lower hydrogen production (Figure 2D). This may also be the cause for the small fluctuations in potential over a period of several days, which are only observed during the illumination periods and not during the dark periods (Figure 2C). Furthermore, Esposito et al. have also clearly shown that, when surface structures are applied, the effect of bubble interference is much less compared to a planar Si surface.[24] As our photoanode is also structured, it therefore probably aids in nucleation and release of bubbles.

For the overall analyses, Döscher et al. proposed four standards in reporting the data of PEC cells:[25] i) Traceable disclosure of the illumination source, which is stated in great detail in the Experimental Section. ii) Thorough device-area definition (including confinement of the illumination area and avoidance of indirect light paths): Our illuminated area of the PEC cell is defined by the opening in the middle of the H-cell, a picture is shown in Figure S8, Supporting Information. Therefore, the surface area of 0.28 cm$^2$ is very well defined and provides no possibility of indirect/parasitic light absorption. iii) Complementary IPCE confirmation of the solar-generation potential: We have published before a full description of the employed PV cell, with corresponding IPCE data.[3] In combination with the the $JV$ measurement of the employed PV cell (Figure 2A), the $JE$ measurement of the device as a photocathode (Figure 2B) and actual hydrogen production data (Figure 2D), which all align in output current density. iv) Proper consideration of faradaic efficiency: Here we follow the standardized procedure

of Coridan et al.[26] to calculate the efficiency of either a PV cell, or an analogous photocathode, or overall PEC performance. We specifically chose to compare the ideal regenerative cell efficiency (photocathode) to the photovoltaic system efficiency, since the input and thus output parameters are similar and therefore easily comparable (as shown in Figure 2A,B).

Others have fabricated photoelectrochemical cells, either wired or wireless for unassisted solar water splitting, however, the combination of long term stability, wireless geometry, and fully separated hydrogen and oxygen production demonstrated here, has never been shown before. When comparing the STH efficiencies and monitored stabilities of fully wireless devices that perform unassisted solar water splitting, examples from literature[7] have shown efficiencies of 2.5–3.2% and stabilities ranging from 4–25 h, while the device reported here has strongly improved performance parameters with a STH efficiency of 7% and a stability of 816 h.

## 2.2. Gas Crossover and pH Gradient Formation in Microporous PEC Devices

The microporous PEC design with catalysts placed on either side of a thin membrane aims to reduce the ion transport path length (in particular of H$^+$) to the microscale, in order to prevent the buildup of a pH gradient that can occur when produced protons need to be transported to the other side around a nonporous device. At the same time, the micropores may pose a risk for if they facilitate gas crossover, resulting in decreased efficiencies and increased safety hazards.

Gas crossover and pH gradient effects were studied using a dummy Si microporous substrate with platinum electrodes on both sides and Nafion embedded in the micropores, as schematically depicted in **Figure 3**A. This design avoids possible limitations imposed by the current-potential characteristics of the triple PV cell in the full PEC device described above. The Si microporous substrate had the same porosity (≈7%) and micropore diameter (50 μm) as the microporous PEC cell with embedded membrane described above. In order to measure the pH near the surface of the device, we constructed a home-made pH meter. The pH was measured near the surface by means of an IrO$_x$ wire versus a reference electrode. The potential of an IrO$_x$ surface depends on the pH of the electrolyte, is very sensitive, has a fast response upon pH change, and is stable over prolonged periods of time and many cycles of pH switching.[27]

The crossover of gaseous products is a major concern for a stand-alone solar-driven water-splitting device. Here, a Nafion membrane was introduced in the micropores, to prevent gas crossover. Figure 3B shows the time evolution of the gas compositions in the anode compartment of two devices, with and without Nafion, as determined by GC measurements. On average ≈6.5% of crossover of H$_2$ into the anode compartment was observed for 100 min of operation when Nafion was not present within the micropores. H$_2$ crossover is most likely due to gas bubbles moving through the open micropores, which results in the observed stepwise increase in concentration of H$_2$ in the anode compartment. In contrast, when Nafion was present in the micropores, only <0.1% crossover of H$_2$ into the anode compartment was observed, which is acceptable from

**ADVANCED
SCIENCE NEWS**

www.advancedsciencenews.com
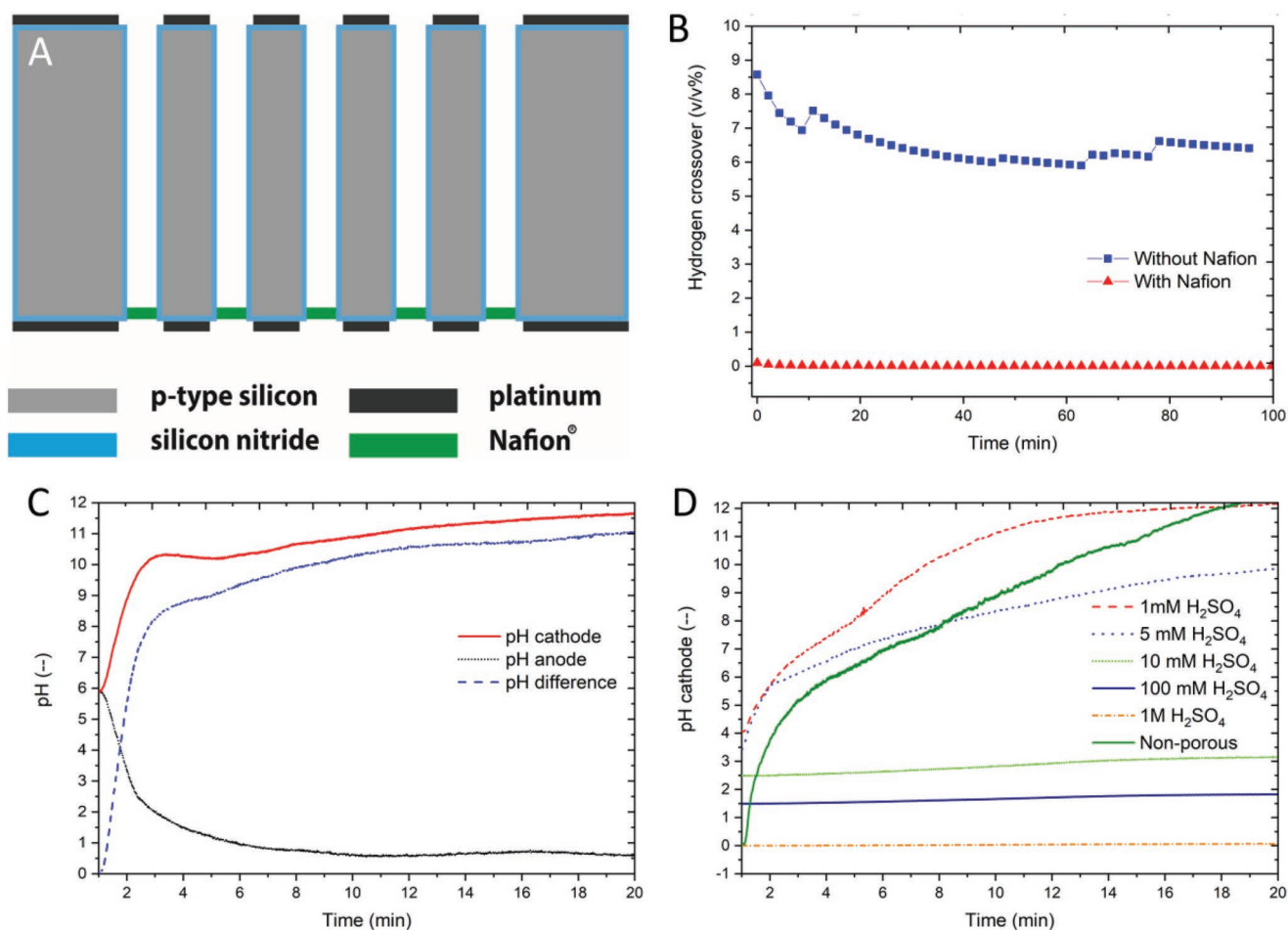
**ADVANCED
ENERGY
MATERIALS**

www.advenergymat.de

**Figure 3.** A) Schematic overview of a microporous dummy electrolysis device for investigating gas crossover and the formation of a pH gradient upon (electrolytic) water splitting. B) Time evolution of the measured hydrogen crossover into the oxygen compartment (anode), with Nafion as molecular barrier (triangle) and without Nafion (square). C) pH in the cathode (solid line) and anode (dotted) compartments, and their difference (dashed), measured over time with Nafion between the anode and cathode in 1 M Na$_2$SO$_4$. D) pH in the cathode compartment over time, for various starting electrolyte compositions, but at a total 1 M electrolyte concentration. Nafion was present between the anode and cathode compartment. Results for a nonporous device operated in 1 M H$_2$SO$_4$ is shown for comparison.

both performance and safety perspectives. The almost two orders of magnitude reduction in crossover values clearly indicates the importance of the incorporation of a molecular barrier in the PEC design.

The occurrence of a concentration overpotential due to the build-up of a pH gradient is a widely investigated topic. As discussed before, a concentration gradient can be resolved by recirculating the anode and cathode compartments, although substantial gas crossover is inevitable in this manner. Here, we investigated the pH gradient formation at a constant electrolyte concentration of 1 M, but with different starting pH. The schematic setup is shown in Figure S9, Supporting Information.

Upon applying a constant current density of 8.13 mA cm$^{-2}$ over the anode and cathode in sodium sulfate electrolyte (i.e., 1 M Na$_2$SO$_4$, pH 5.8), the pH at the cathode rapidly increased within minutes to a pH of ≈11, see Figure 3C. Within the same time the pH decreased at the anode to a very low value of ≈0.7. Within minutes, a pH gradient of more than ten units was established over the device. Such a difference would lead to an increase in potential required to drive the complete PEC cell

of >590 mV. The large induced overpotential is attributed to the conductance through the electrolyte, in which the majority of carriers will be Na$^+$ and SO$_4^{2-}$, and not the produced or consumed protons. Therefore, a depletion and accumulation of protons will occur in the anode and cathode compartments, respectively. For comparison, the catalytic overpotentials for highly active catalysts, such as IrO$_x$ for the OER and Pt for the HER in acidic electrolyte as they were benchmarked by McCrory et al., were 360 and 52 mV, respectively.[4] The above analysis demonstrates that the potential loss due a pH gradient may easily become the limiting factor in PEC performance.

By decreasing the starting pH, an increase in the transport of protons is expected, and therefore a decrease of the built-up pH gradient. We tested different electrolyte composition of Na$_2$SO$_4$ and H$_2$SO$_4$, keeping the overall sulfate concentration at 1 M. Figure 3D shows the results of the pH change over time, with different starting compositions as stated by the specific concentrations of H$_2$SO$_4$. For comparison, results for a nonporous device are shown as well, for which the anode and cathode compartments were connected by a salt bridge. These

results corroborate those of the wireless PEC device of Reece et al., who concluded that a pH gradient between the cathode and anode compartments was the reason for the observed rapid loss of performance.[7] Upon lowering the starting pH, a longer period of time was required before depletion of protons in the cathode compartment became evident. Even for 0.9 M Na₂SO₄ and 0.1 M H₂SO₄ a pH increase of 0.3 units was measured after 20 min. Not until a pure electrolyte of 1 M H₂SO₄ was used, a stable pH over time was observed, as is seen in Figure 3D. The importance of the implementation of micropores in the device is further underscored by the change in pH observed for a nonporous device operated in 1 M H₂SO₄. After only 20 min of operation, already a substantial increase in pH was observed. This observation agrees with the findings of Modestino et al.[13] Our results indicate that the produced/consumed ion needs to be the major charge carrier when the build-up of a gradient is to be prevented. We tested also lower concentrations of H₂SO₄ in the absence of Na₂SO₄ (data not shown), but in this case the lower electrolyte conductance became problematic.

## 2.3. Simulating pH Gradient Formation

To gain more insight in the development of a pH gradient, an analytical and a computational COMSOL model were developed. A simple model already provides insight into the evolution of a pH gradient over the anode and cathode compartment. In order to estimate the length scale at which pH gradient formation becomes an issue, a 1D, infinite parallel plate model was developed, in which an electrolyte is placed between cathode and anode and a steady-state proton gradient was established. In this case, 1D Fick's first law in steady state can be used, which simplifies to Equation (1).

$$J = -D\frac{\Delta C}{x} \tag{1}$$

Here $J$ is the proton flux, $D$ is the diffusion constant of protons, $x$ is the distance between the electrodes and $\Delta C$ is the proton concentration difference between anode and cathode. Here, the proton flux is directly related to the operating current density ($J_{op}$), and therefore the proton concentration is given by Equation (2).

$$\Delta C = \frac{J_{op}x}{DF} \tag{2}$$

Here $F$ is the Faraday constant. The concentration gradient cannot be more than twice the electrolyte concentration ($C_{el}$), and therefore the critical dimension, $x_{crit}$, at which the concentration at the anode becomes zero, is given by

$$x_{crit} = \frac{2C_{el}F}{J_{op}} \tag{3}$$

At an operating current density of 8.13 mA cm⁻² (i.e., 10% STH efficiency) and an electrolyte proton concentration of 0.1 M, $x_{crit}$ is ≈2 mm. However, a zero proton concentration at the cathode would result in an infinite overpotential. When

allowing an overpotential in the order of the kinetic overpotential required for Pt to produce hydrogen (52 mV), a separation distance of ≈1.7 mm is allowed. When the proton concentration of the electrolyte is reduced, the maximum electrode separation to allow the same overpotential is reduced with the same factor, that is, a $C_{el}$ of 0.01 M results in a ≈170 μm maximum separation distance. Most operational lab-scale PEC devices are constructed with dimensions on the order of 1 cm², with macroscopic slits at the sides through which the electrolyte solutions in either compartment can mix. This analytical model already highlights one of the major problems: the proton transport between the anode and cathode compartments needs to be in the micrometer-scale in order to avoid major overpotentials due to gradient build-up.

The above described model assumes parallel plates and only diffusion of protons. This model includes neither the migration of protons in an electric field, nor the fact that anode and cathode are not parallel, as is the case in a real PEC device, in particular a wireless one. To gain more insight in the geometric design parameters, a 2D COMSOL model, which includes elements of the actual device geometry which can be fabricated (i.e., wafer thickness, pore diameter, and pore distribution), diffusion, and migration, was developed to assess the pH gradient formation. First, a nonporous setup found in literature was simulated, as is shown in **Figure 4**A.[28] During (simulated) operation, a pH gradient develops near the surfaces of the electrodes. Figure 4A shows the calculated pH profile for the system after 15 min of simulated operation at 8.13 mA cm⁻² with a starting H⁺ concentration of 0.1 M. Although the electrolyte was a strong acid, the pH at the surface of the cathode was around ≈8.5, and the pH at the surface of the anode was ≈0.7. The simulation shows great similarities with simulations done by Jin et al., who performed it at near-neutral pH.[28] The average potential loss due to such a pH gradient would be 462 mV (i.e., 59 mV/pH-unit per decade).

By introducing microslits (slits with a width of 50 μm) in the device with a certain pitch, a pH gradient can be suppressed, by reducing the distance over which protons are transported. A similar simulation was performed as described above, but now several microslits (e.g., 60 slits per centimeter) were introduced in the system. Figure 4B shows the results after 15 min of simulated operating time. A substantial decrease in pH gradient was observed within the system. The pH at the anode and cathode, simulated at the electrode surfaces (see green dots in Figure 4D), were ≈0.80 and ≈1.2, respectively. This almost completely suppressed gradient is mainly attributed to a shortened proton transport distance from the anode to the cathode. More insight is generated by changing the density of microslits in the system. From Figure 4C it becomes clear that from 60 microslits per centimeter a steady state pH is obtained after ≈10 min of simulated operating time. Increasing the density of microslits (e.g., 100 microslits per centimeter) does not lead to further significant decrease of the pH at the cathode. The above modeled system is 2D (i.e., microslits instead of micropores), but it indicates again, as seen for the 1D analytical model as well, that the shortest distance between the electrodes is of crucial importance. Therefore, in an actual, 3D PEC cell micropores can offer such diffusion short-cuts, and at a much lower overall porosity than microslits, for example, a microslit of 50 μm width and
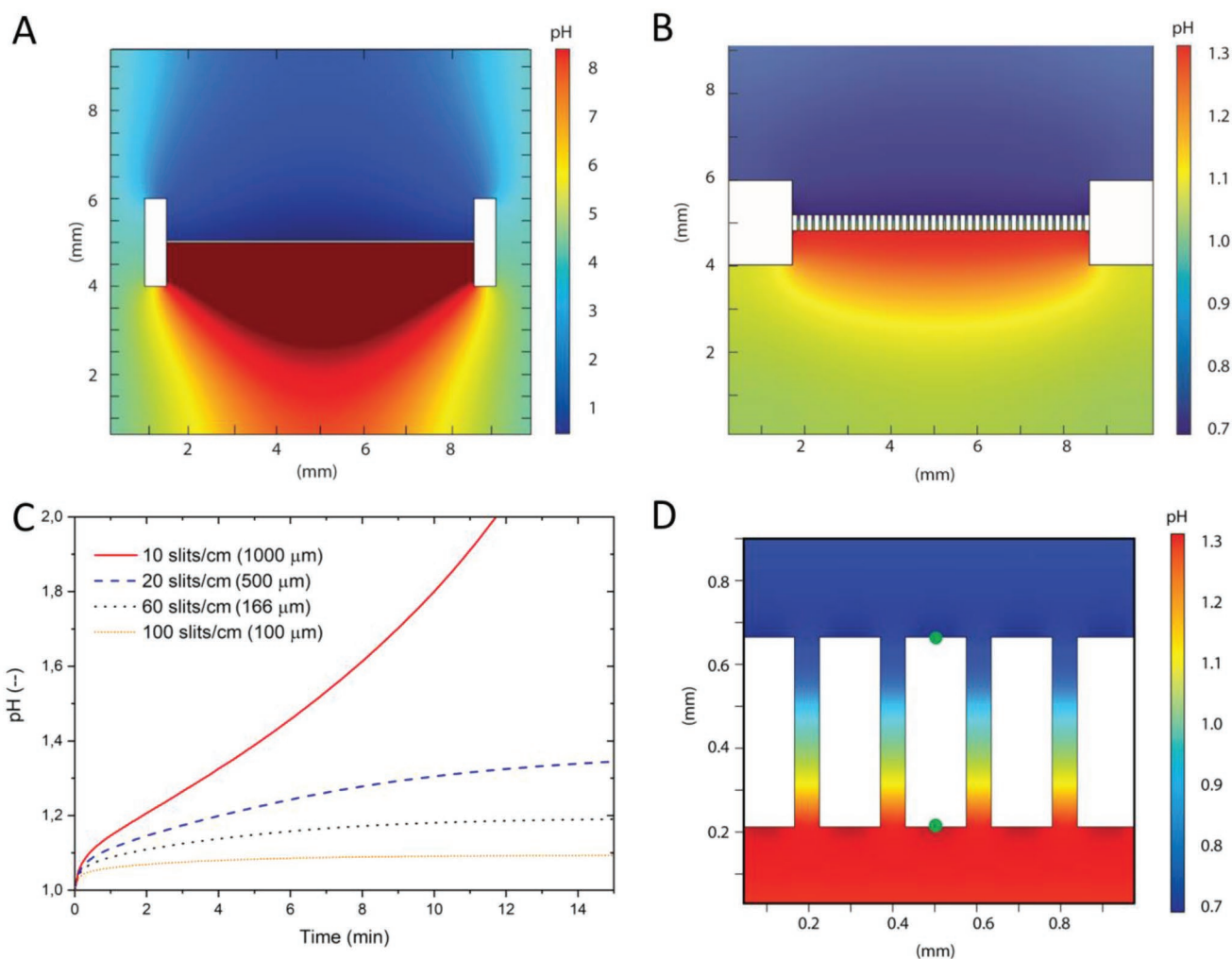
**ADVANCED
SCIENCE NEWS**
www.advancedsciencenews.com

**ADVANCED
ENERGY
MATERIALS**
www.advenergymat.de

**Figure 4.** Cross-sectional pH profiles in the A) nonmicroporous PEC device and B) in a microporous device with 60 slits/cm from COMSOL Multiphysics 2D simulations after 15 min operation at 8.13 mA cm$^{-2}$ starting in homogeneous 0.1 M H$_2$SO$_4$. C) Simulated pH over time at one of the cathode slits for different numbers of microslits within the device. D) Zoom in of (B) near the membrane.

166 µm pitch would result in a 30% porosity, and thus 30% less light absorption. In contrast, micropores of 50 and 166 µm pitch, which provide the same H$^+$ transport path length, result in 7% porosity, and thus only 7% less light absorption. Moreover, both the simulations and measurements show the importance of porosity and the use of an electrolyte with a high concentration of protons for the device stability during operation.

The most important lesson resulting from both simulations is that the proton diffusion distance between cathode and anode is the crucial device parameter. If the distance is too long, a pH gradient will build up that causes a detrimental overpotential. In practice in our microporous PEC cell design, the distance is primarily governed by the micropore density, although the membrane thickness also plays a role. All in all, both models provide basic design rules for a well-performing microporous PEC device: i) at highly acidic electrolytes, micropore separations can be on the order of 100 µm; a higher degree of porosity is unnecessary and even undesired because this would give a loss of photoabsorber volume; ii) more weakly acidic electrolytes have concomitantly more stringent design requirements.

## 3. Conclusion

We have designed, fabricated, and experimentally validated a membrane-embedded microporous PEC cell architecture that prevents the ionic transport losses, the formation of a pH gradient, and gas crossover in a PEC cell. By introducing micropores into a Si triple cell, all three losses have been suppressed and kept within the limit of 250 mV. Together with the research of Bosserez et al. and our performed simulation on pH gradient formation, we conclude that a micropore pitch <250 µm is required, and an overall porosity of ≈7% ensures low ionic losses of <100 mV in acidic electrolyte conditions.[10] Therefore, our final device was constructed of micropores with a diameter of 50 µm and a pitch of 166 µm. Crossover of the co-evolved gasses (i.e., H$_2$ and O$_2$) was prevented by the incorporation of Nafion proton exchange membrane within the micropores, which brought the gas crossover down to well below safety guidelines.

The formation of a pH gradient between the anode and cathode compartment in 1 M Na$_2$SO$_4$ was observed within

minutes of operation, thereby increasing the voltage available for water splitting by >500 mV. By increasing the initial acidity of the electrolyte to a pH of 2.5, a significant decrease in pH gradient was observed, however it still increased over time. Not until a pure electrolyte of 1 M $H_2SO_4$ was employed, the pH remained stable over time.

A fully stand-alone PEC cell was fabricated according to these design principles. We have demonstrated that, by careful design at the microscale, the chosen architecture provides a high performance. The micropore concept should also be applicable to other material combinations, provided that fabrication methods can be found to achieve similar structuring at the right scale. The best-performing stand-alone microporous membrane-embedded PEC cell investigated here demonstrated a STH efficiency of ≈7%.

Our future research will focus on the incorporation of all earth-abundant materials, especially for the chosen catalyst materials. Furthermore, as shown by McCrory et al. by benchmarking several OER catalysts, the activity of the OER catalyst is higher in alkaline electrolyte.[4] The currently shown microporous PEC cell is unstable in alkaline electrolyte, due to the bare Si surface that is exposed in the pores, which etches rapidly in alkaline medium. Therefore, the stability of the present microporous PEC cell should be increased for alkaline conditions.

## 4. Experimental Section

*Triple PV Cell Fabrication*: The triple PV cell structure consists of a hybrid thin film a-Si:H/nc-Si:H tandem deposited on top of a silicon heterojunction cell (SHJ), resulting in a triple junction. The polished c-Si wafers (Topsil, n-type, <111> FZ, ≈280 μm), were cleaned using a sequence of 99% $HNO_3$ at room temperature for 10 min, 69.5% $HNO_3$ at 95 °C for 10 min. Subsequently, a dip in 0.55% HF was performed at room temperature to remove the oxide film. The thin film silicon layers were fabricated in a multichamber Elettrorava equipment by plasma enhanced chemical vapor deposition (PECVD). Silane ($SiH_4$), hydrogen ($H_2$), carbon dioxide ($CO_2$), phosphine ($PH_3$), and diborane ($B_2H_6$) were used as precursor gases. The p- and n-layers of the p-i-n junctions are based on doped nanocrystalline silicon oxide (nc-$SiO_x$:H), nanocrystalline silicon (nc-Si:H), and amorphous silicon (a-Si:H). A highly doped layer was used as the tunneling recombination junction between the nc-Si:H and SHJ cells, by increasing the phosphine flow by 50% with respect to the standard flows.

*Catalyst Deposition*: A transparent conductive oxide, hydrogenated indium oxide (IOH), was sputtered on both sides of the finished triple junction cell, in order to improve the charge extraction from the underlying materials. The deposition was conducted at room temperature with a power of 135 W and 30 μbar of $H_2O$ partial pressure, and then annealed at 175 °C for 150 min.

Iridium (Ir) microdots were patterned by means of lift off. squares (10 × 10 mm²) with cubic packed circles (2 μm diameter, varying pitch) were defined in a positive photoresist polymer (Olin 906–12). Ir was deposited by means of an in-house built sputter device. The silicon wafer was placed on a rotating chuck (5 rpm), 44 mm from the Ir source, in a low-pressure reactor chamber (5.5 × 10⁻³ mbar) with a 40 sccm flow of argon from the bottom of the chamber. The Ir source had an angle of 45° with respect to the wafer surface. Ir was sputtered at a 2.6 nm min⁻¹ deposition rate by means of a DC power of 50 W and a 20 sccm argon flow at the gun, for 20 min. Subsequently, microdots were obtained by lift-off, by immersing the wafer in acetone in an ultrasonic bath for 20 min, followed by immersing the wafer in iso-propanol, in an ultrasonic bath for 20 min. The electrochemical growth of $IrO_x$ from Ir was carried

out in a 0.5 M $H_2SO_4$ solution with a Versastat 4 potentiostat. For a 0.5 M $H_2SO_4$ solution, the optimal switching potentials are $V_U = 1.25$ V and $V_L = -0.25$V versus RHE, a sweeping rate of 150 mV s⁻¹, for a time of 20 s.[27a] In case of the characterization of fully or partially covered Ir substrates, n++-Si (CZ, n++-type, <110> CZ, ≈380 μm) was used either without patterning or with patterning as described above.

The backside of the substrate was completely covered with a Pt layer, sputtered by means of an in-house built sputter system. The silicon wafer was placed on a rotating chuck (5 rpm), 44 mm from the Pt source, in a low-pressure reactor chamber 6.6 × 10⁻³ mbar) with a 145 sccm flow of argon. The Pt source had an angle of 45° with respect to the wafer surface. By means of a DC power of 200 W Pt was sputtered (5.0 nm min⁻¹ deposition rate), for 10 min.

*Micropore Formation by Deep Reactive Ion Etching*: By means of standard photolithography, squares (10 × 10 mm²) with cubic packed circles (50 μm diameter, 166 μm pitch) were defined in a photoresist polymer (Olin 908–35). First the IOH on the front side of the wafer was removed by reactive ion etching (RIE, Adixen AMS100DE), directly followed by the fabrication of silicon micropores (≈280 μm deep). These were etched into the silicon substrate by deep reactive ion etching (DRIE, Adixen AMS100SE, $SF_6$ and $C_4F_8$ pulsed process) and the substrates were cleaned subsequently in oxygen plasma (30 min) and a Piranha solution (20 min) to remove the photoresist and fluorocarbon residues.

*Embedding of Ion Exchange Material*: 10 mL Nafion solution (20 wt%, Sigma-Aldrich) was added to 10 mL dimethylformamide (DMF). By evaporation at a rotavap, at 10⁻³ mbar and 80 °C the lower aliphatic alcohols and water content were removed. 100 μL was dropcast at the backside of a microporous structure and dried at a hotplate of 60 °C. After solvent evaporation, Nafion covering the Pt backside was removed by a razor blade, thereby leaving only the Nafion that closes off the micropores.

*Fabrication of the pH Gradient Test Cell*: The test cell for assessment of the formation of a pH gradient was fabricated from a n-type silicon <100> substrate (1–10 Ω cm, 380 μm thickness, single side polished, Okmetic Finland). First, micropores were etched through the wafer as stated above. Hereafter, the substrates were covered with 100 nm silicon nitride ($SiN_x$). A double (front and back) second patterning step was employed to create a ring of $SiN_x$ around each micropore by standard photolithography (Olin 907-17 photoresist), see Figure S10A, Supporting Information. Pt was sputtered over the entire sample (front and back), with settings as stated above for Pt sputtering. Subsequently, microrings were obtained by lift-off, by immersing the wafer in acetone in an ultrasonic bath for 20 min, followed by immersing the wafer in iso-propanol in an ultrasonic bath for 20 min (see Figure S10B, Supporting Information). The microrings around the micropores ensured electrical isolation between front and back, which is important for their use as separate electrodes. A Nafion membrane was applied as stated above (see Figure S10C, Supporting Information).

*JV Measurements of the PV Cells*: To measure the electrical characteristics of the Si microporous membrane, the anode side was positioned perpendicular to a light source. Ir was contacted as the working electrode and Pt as the counter electrode, in a 4-electrode setup. *JV* measurements were recorded on a VersaSTAT 4 potentiostat using a linear voltage sweep from −2 to 2V at a rate of 0.2 V s⁻¹. The light intensity was calibrated to AM 1.5G illumination at the position of the sample, using the calibrated light source described below. Every curve is the average of five consecutive forward sweeps.

*JE Measurements of the Photocathode*: For the characterization of the device as a photocathode, as presented in Figure 2B and schematically in Figure S2, Supporting Information, the device was contacted at the illuminated frontside as working electrode (WE), a platina mesh as counter electrode (CE), and a Ag/AgCl reference electrode (RE) was within the cathode compartment. The electrolyte used was a 1 M aqueous sulfuric acid ($H_2SO_4$). Five full cyclic voltammetry measurements between −0.05 and 2 V versus RHE were done at a scan rate of 10 mV s⁻¹ and the averages of five forward sweeps are reported. Samples were positioned perpendicular to a solar spectrum light source. The light intensity was calibrated to AM 1.5G illumination at the position

**ADVANCED
SCIENCE NEWS**

www.advancedsciencenews.com

**ADVANCED
ENERGY
MATERIALS**

www.advenergymat.de

of the sample as is described below and in more detail elsewhere.[23] The compartment was stirred during the measurement, in order to decrease bubble formation at the cathode.

*JE Measurements of the IrOₓ Micropatterned Anode*: For *JE* measurements of the anode as presented in Figure 2D and Figure S4, Supporting Information (schematic setup in Figure S5, Supporting Information), the substrate was contacted at the backside side as working electrode. A platinum mesh served as counter electrode (CE) and an Ag/AgCl as reference electrode (RE). The electrolyte used was 1 M aqueous sulfuric acid ($H_2SO_4$). Five full cyclic voltammetry measurements between 1.4 and 1.9 V versus RHE were performed at a scan rate of 10 mV s$^{-1}$, and the averages of five forward sweeps are reported. The compartment was stirred during the measurement, in order to decrease bubble formation at the anode.

*JE Measurements of the Photoanode*: For the characterization of the device as a photoanode as presented in Figure S6, Supporting Information (schematic setup in Figure S7, Supporting Information), the cathode was contacted through the Pt contact on the back side as working electrode (WE), a platina mesh as counter electrode (CE), and a Ag/AgCl reference electrode (RE) was within the anode compartment. The electrolyte used was 1 M aqueous sulfuric acid ($H_2SO_4$). Five full cyclic voltammetry measurements between −0.05 and 2 V versus RHE were done at a scan rate of 10 mV s$^{-1}$, and the average of five forward sweeps is reported. Samples were positioned perpendicular to a solar spectrum light source, and the light was passed through the electrolyte in the anode compartment. The light intensity was calibrated to AM 1.5G illumination at the position of the sample as is described below and in more detail elsewhere.[23] The compartment was stirred during the measurement, in order to decrease bubble formation at the cathode.

*JE Measurements of the Full Water Splitting PEC Device during Stability Testing*: For the characterization of the stability of the stand-alone PEC water splitting cell as presented in Figure 2C, a setup was used as schematically depicted in Figure S3, Supporting Information, and Figure S8, Supporting Information, depicts photographs of the actual H-cell. The (photo)anode side was contacted at the illuminated frontside as working electrode (WE), the full Pt backside as counter electrode (CE), and an Ag/AgCl reference electrode (RE) was within the anode compartment. The electrolyte used was a 1 M aqueous sulfuric acid ($H_2SO_4$). The measurement was done in open circuit mode, therefore the potentiostat only recorded the potential difference between the WE and CE (i.e., the input impedance of the potentiostat is much higher than the overall resistance of the PEC cell, >10$^9$ Ω). The sample rate was every 35 s for 40 days. A sample was positioned perpendicular to a solar spectrum light source. The light intensity was calibrated to AM 1.5G illumination at the position of the sample as is described below and in more detail elsewhere.[23] A shutter controlled the switching of the lamp in a 8 h/16 h on/off cycle. The compartments were stirred during the measurement, in order to decrease bubble formation at the cathode and anode sides of the device.

The water layer on top of the sample was ≈15 mm thick. The absolute light absorption by the solution would lead to a decrease of 4 mA cm$^{-2}$ if it is assumed that every photon leads to an electron.[23] The absorption was calculated by the Lambert–Beer relation and integrated over the solar spectrum in the range of 300–1200 nm, which is in agreement with the data presented by Döscher et al.[29] The data clearly indicate that water starts to absorb light from 950 nm and above. When looked at the IPCE data of our employed PV cell,[3] the top cell generates ≈8.6 mA cm$^{-2}$, the middle cell ≈9.2 mA cm$^{-2}$, and the bottom cell ≈17.1 mA cm$^{-2}$. The employed middle cells absorb light till ≈900 nm, therefore only the bottom cell is affected by the water layer, however produces more than enough current to compensate in the current matching.

*Gas Detection*: The reactor was connected to a gas chromatograph (GC, Compact GC, Interscience), equipped with a Parabond Q column (10 m) and a TCD detector to determine the amount of $H_2$ in the argon carrier gas. A flow of 10 mL min$^{-1}$ argon was introduced into the electrolyte which was sampled every 130 s for the presence of $H_2$. The carrier gas and detector were calibrated for $H_2$ detection, therefore it was not possible to simultaneously detect $O_2$. The carrier gas was

flushed at the same rate through the oxygen compartment, in order to keep the pressure in both compartments equal. A schematic illustration of the setup is given in Figure S11, Supporting Information, and pictures of the used H-cell are given in Figure S8, Supporting Information.

*JE Measurements of the Microporous Dummy Electrolysis Device*: The Si microporous membranes, with Pt at both sides as made for assessment of the pH gradients, were photoelectrochemically tested using a potentiostat (VersaSTAT 4) in a three-electrode configuration, where the anode with an exposed projected surface area of 0.28 cm$^2$ acted as the working electrode (WE), the backside was contacted as counter electrode (CE), an Ag/AgCl electrode as the reference electrode (RE), and a oxidized Ir wire as secondary electrode (SE), as illustrated in Figure S9, Supporting Information, and the actual H-cell as depicted in Figure S8, Supporting Information. The electrolyte used was either 1 M aqueous sulfuric acid ($H_2SO_4$), or a dilution thereof to which $Na_2SO_4$ was added to maintain an overall sulfate concentration of 1 M, as stated above (e.g., 0.1 $H_2SO_4$ + 0.9 M $Na_2SO_4$, 10 mM $H_2SO_4$, and 990 mM $Na_2SO_4$, see Figure 3D). No adjustment was made for the electrolyte resistance (≈0.08 Ω), since this is only a small contribution compared to the contact resistance of ≈1 Ω cm$^{-2}$. Five full cyclic voltammetry measurements were done at a scan rate of 10 mV s$^{-1}$ and the averages of five forward sweeps are reported.

*Light Source and Calibration*: The light source that was used is a 300 W xenon arc light source, fitted with Air Mass filter (AM 1.5 G) from Newport, Oriel Instruments. Upon installation, the lamp was calibrated by Newport. Before every measurement the lamp was checked by a calibrated reference solar cell (91150V). The 91150V reference cell and meter consists of a readout device and a 2 × 2 cm calibrated solar cell made of monocrystalline silicon and a KG5 window. The cell is equipped with a thermocouple assembled in accordance with IEC 60904-2. The certification is accredited by NIST to the ISO-17025 standard. It reads solar simulator irradiance in sun units, whereby one sun is equal to 1000 W m$^{-2}$ at 25 °C and AM 1.5 Global Reference.

The solar simulator was checked for spectral mismatch by a spectrometer (AvaSpec-ULS2048XL-EVO) fitted with a CC-VIS/NIR, slit size of 10 μm, 1.4 nm resolution in the range of 300–1050 nm, an integration time of 8 ms, and averaged over 60 scans.

*COMSOL Modeling*: Numerical simulation of the system was performed by COMSOL 5.3, by means of the electrochemistry module in 2D (A typical geometry is given in Figure 4B), with as main model the tertiary current. The net molar flux of each species in the electrolyte, $N_i$, is the sum of the fluxes due to migration, diffusion, and convection, such that

$$N_i = -D_i\nabla c_i - z_iu_iFc_i\nabla\varnothing_l + vc_i \tag{4}$$

where $\varphi_l$ is the electric potential, $v$ is the velocity, $c_i$ is the concentration, $D_i$ is the diffusion coefficient, $z_i$ is the charge number, $u_i = D_i/RT$ is the mobility where $R$ is the ideal gas constant and $T$ is the absolute temperature, and $F$ is the Faraday constant. The conservation of mass requires that

$$R_i = \frac{\partial c_i}{\partial t} + \nabla \cdot \mathbf{N}_i \tag{5}$$

where $R_i$ is the net rate of formation of the $i$th species due to bulk ionic reactions such as buffer and water-dissociation kinetics. The predominant source of convection in this system was due to product bubbles, an effect that was neglected in the modeling. Electroneutrality was assumed at every point in the simulation space, such that

$$\sum_{i=l}^{n} z_ic_i = 0 \tag{6}$$

The charge-transfer kinetics at the electrodes were represented according to the Butler–Volmer model as

$$\mathbf{n} \cdot i_l = i_R = i_0 \left[ e^{\frac{\alpha_aF(\varnothing_s-\varnothing_l-E_0)}{RT}} - e^{\frac{\alpha_cF(\varnothing_s-\varnothing_l-E_0)}{RT}} \right] \tag{7}$$

The values used in the simulations are listed in **Table 2** below.[5a]

**Table 2.** Parameters used in the COMSOL simulations.

| Parameter | Description | Value |
|---|---|---|
| $i_0$ (OER) | OER exchange current density | $1.4 \times 10^{-8}$ A cm$^{-2}$ |
| $\alpha_a$ (OER) | OER anodic transfer coefficient | 1.7 |
| $\alpha_c$ (OER) | OER cathodic transfer coefficient | 0.1 |
| $i_0$ (HER) | HER exchange current density | $1 \times 10^{-3}$ A cm$^{-2}$ |
| $\alpha_a$ (HER) | HER anodic transfer coefficient | 1 |
| $\alpha_c$ (HER) | HER cathodic transfer coefficient | 1 |
| $E_0$ | Equilibrium potential | 1.229 V |
| $T$ | Reaction temperature | 298 K |
| $D_{H^+}$ | Diffusion coefficient H$^+$ | $9.3 \times 10^{-5}$ cm$^2$ s$^{-1}$ |
| $D_{HSO_4^-}$ | Diffusion coefficient HSO$_4^-$ | $1.3 \times 10^{-5}$ cm$^2$ s$^{-1}$ |
| $D_{na^+}$ | Diffusion coefficient Na$^+$ | $1.9 \times 10^{-5}$ cm$^2$ s$^{-1}$ |
| $D_{SO_4^{2-}}$ | Diffusion coefficient SO$_4^{2-}$ | $1.0 \times 10^{-5}$ cm$^2$ s$^{-1}$ |
| $I_{lim}$ | Limiting photocurrent | 20 mA cm$^{-2}$ |
| $S_w$ | Conductivity electrolyte | 0.5 S cm$^{-1}$ |

## Supporting Information

Supporting Information is available from the Wiley Online Library or from the author.

## Conflict of Interest

The authors declare no conflict of interest.

[1] M. R. Singh, K. Papadantonakis, C. Xiang, N. S. Lewis, *Energy Environ. Sci.* **2015**, *8*, 2760.

[2] a) M. G. Walter, E. L. Warren, J. R. McKone, S. W. Boettcher, Q. Mi, E. A. Santori, N. S. Lewis, *Chem. Rev.* **2010**, *110*, 6446; b) T. Shinagawa, K. Takanabe, *ChemSusChem* **2017**, *10*, 1318.

[3] P. Perez-Rodriguez, W. Vijselaar, J. Huskens, M. Stam, M. Falkenberg, M. Zeman, W. Smith, A. H. M. Smets, *Prog. Photovoltaics* **2019**, *27*, 245.

[4] C. C. McCrory, S. Jung, I. M. Ferrer, S. M. Chatman, J. C. Peters, T. F. Jaramillo, *J. Am. Chem. Soc.* **2015**, *137*, 4347.

[5] a) S. Haussener, C. Xiang, J. M. Spurgeon, S. Ardo, N. S. Lewis, A. Z. Weber, *Energy Environ. Sci.* **2012**, *5*, 9922; b) S. Haussener, S. Hu, C. Xiang, A. Z. Weber, N. S. Lewis, *Energy Environ. Sci.* **2013**, *6*, 3605; c) S. Hu, C. Xiang, S. Haussener, A. D. Berger, N. S. Lewis, *Energy Environ. Sci.* **2013**, *6*, 2984; d) C. Xiang, A. Z. Weber, S. Ardo, A. Berger, Y. Chen, R. Coridan, K. T. Fountaine, S. Haussener, S. Hu, R. Liu, N. S. Lewis, M. A. Modestino, M. M. Shaner, M. R. Singh, J. C. Stevens, K. Sun, K. Walczak, *Angew. Chem., Int. Ed.* **2016**, *55*, 12974.

[6] J. Ronge, T. Bosserez, D. Martel, C. Nervi, L. Boarino, F. Taulelle, G. Decher, S. Bordiga, J. A. Martens, *Chem. Soc. Rev.* **2014**, *43*, 7963.

[7] S. Y. Reece, J. A. Hamel, K. Sung, T. D. Jarvi, A. J. Esswein, J. J. H. Pijpers, D. G. Nocera, *Science* **2011**, *334*, 645.

[8] J. Newman, *J. Electrochem. Soc.* **2013**, *160*, F309.

[9] a) R. L. LeRoy, M. B. I. Janjua, R. Renaud, U. Leuenberger, *J. Electrochem. Soc.* **1979**, *126*, 1674; b) S. K. Mazloomi, N. Sulaiman, *Renewable Sustainable Energy Rev.* **2012**, *16*, 4257.

[10] T. Bosserez, L. Geerts, J. Rongé, F. Ceyssens, S. Haussener, R. Puers, J. A. Martens, *J. Phys. Chem. C* **2016**, *120*, 21242.

[11] Environmental Chemistry, Periodic Table of Elements: Element Hydrogen (H$_2$), https://environmentalchemistry.com/yogi/periodic/H.html (accessed: April 2017).

[12] E. A. Hernandez-Pagan, N. M. Vargas-Barbosa, T. Wang, Y. Zhao, E. S. Smotkin, T. E. Mallouk, *Energy Environ. Sci.* **2012**, *5*, 7582.

[13] M. A. Modestino, K. A. Walczak, A. Berger, C. M. Evans, S. Haussener, C. Koval, J. S. Newman, J. W. Ager, R. A. Segalman, *Energy Environ. Sci.* **2014**, *7*, 297.

[14] Y. K. Chen, K. Sun, H. Audesirk, C. X. Xiang, N. S. Lewis, *Energy Environ. Sci.* **2015**, *8*, 1736.

[15] C. Trompoukis, A. Abass, J.-W. Schüttauf, T. Bosserez, J. Rongé, J. Lauwaert, J. A. Martens, R. Baets, *Sol. Energy Mater. Sol. Cells* **2018**, *182*, 196.

[16] P. Perez-Rodriguez, I. Digdaya, A. M. Raventos, M. Falkenberg, R. Vasudevan, M. Zeman, W. Smith, A. H. M. Smets, *Proc. 2016 IEEE 43rd Photovol. Spec. Conf.* **2016**, *7*, 3620.

[17] K. P. Rola, I. Zubel, *Mater. Sci.-Pol.* **2011**, *29*, 278.

[18] a) C. Heitner-Wirguin, *J. Membr. Sci.* **1996**, *120*, 1; b) N. Wehkamp, M. Breitwieser, A. Buchler, M. Klingele, R. Zengerle, S. Thiele, *RSC Adv.* **2016**, *6*, 24261.

[19] R. Elbersen, R. M. Tiggelaar, A. Milbrat, G. Mul, H. Gardeniers, J. Huskens, *Adv. Energy Mater.* **2015**, *5*, 1401745.

[20] S. Schaefer, R. Lüdemann, *J. Vac. Sci. Technol., A* **1999**, *17*, 749.

[21] G. Dingemans, R. Seguin, P. Engelhart, M. C. M. van de Sanden, W. M. M. Kessels, *Phys. Status Solidi (RRL)* **2010**, *4*, 10.

[22] K. Imamura, M. Takahashi, Asuha, Y. Hirayama, S. Imai, H. Kobayashi, *J. Appl. Phys.* **2010**, *107*, 054503.

[23] W. Vijselaar, P. Westerik, J. Veerbeek, R. M. Tiggelaar, E. Berenschot, N. R. Tas, H. Gardeniers, J. Huskens, *Nat. Energy* **2018**, *3*, 185.

[24] D. V. Esposito, Y. Lee, H. Yoon, P. M. Haney, N. Y. Labrador, T. P. Moffat, A. A. Talin, V. A. Szalai, *Sustainable Energy Fuels* **2017**, *1*, 154.

[25] H. Döscher, J. L. Young, J. F. Geisz, J. A. Turner, T. G. Deutsch, *Energy Environ. Sci.* **2016**, *9*, 74.

[26] R. H. Coridan, A. C. Nielander, S. A. Francis, M. T. McDowell, V. Dix, S. M. Chatman, N. S. Lewis, *Energy Environ. Sci.* **2015**, *8*, 2886.

[27] a) W. Olthuis, J. C. van Kerkhof, P. Bergveld, M. Bos, W. E. van der Linden, *Sens. Actuators, B* **1991**, *4*, 151; b) K. G. Kreider, M. J. Tarlov, J. P. Cline, *Sens. Actuators, B* **1995**, *28*, 167.

[28] J. Jin, K. Walczak, M. R. Singh, C. Karp, N. S. Lewis, C. Xiang, *Energy Environ. Sci.* **2014**, *7*, 3371.

[29] a) G. M. Hale, M. R. Querry, *Appl. Opt.* **1973**, *12*, 555; b) H. Döscher, J. F. Geisz, T. G. Deutsch, J. A. Turner, *Energy Environ. Sci.* **2014**, *7*, 2951.